Available online at www.sciencedirect.com
ScienceDirect
Sensors and Actuators A 132 (2006) 597–606
SENSORS AND ACTUATORS A PHYSICAL
www.elsevier.com/locate/sna

Analysis of filling of an oval disk-shaped chamber with microfluidic flows

J.J. Chen [a,*], W.Z. Liu [b], J.D. Lin [b], J.W. Wu [a]

[a] *Industrial Technology Research Institute, 195 Sec. 4, Chung Hsing Road, Chutung, Hsinchu 310, Taiwan, ROC*
[b] *Department of Mechanical Engineering, National Chiao Tung University, 1001 Ta Hsueh Road, Hsinchu 300, Taiwan, ROC*

Received 6 January 2005; received in revised form 8 March 2006; accepted 9 March 2006
Available online 17 April 2006

Abstract

The filling of an oval disk-shaped micro-chamber by liquid is analyzed with reference to micro-systems with inlets and outlets of various widths, which are fabricated using MEMS technology. The results concern the motion of the gas–liquid interface. The flow fields during the filling of the micro-chambers are also studied. During the filling, the front shape is determined by the competition among inertia, adhesion and surface tension. The effects of non-dimensional parameters, such as the Reynolds number and the Weber number, both determine by the inlet velocity, as well as the wall adhesive conditions, on the flow characteristics are examined. The effects of the widths of channels in a circular chamber and the lengths of the semi-major and semi-minor axes of an oval chamber on the filling process are also investigated. Geometric changes alter the angle between the microchannels and the micro-chamber at their intersection and significantly affect the filling of the micro-chamber with the liquid. The location of bubble entrapment is plotted parametrically against the Weber number, the liquid/substrate contact angle and the change in the angle between the microchannels and the micro-chamber at intersection. Evidently, air is entrapped when the inertia is high, large changes in the angle between the channels and the chamber at the intersection are made, and a hydrophobic property is observed inside the chamber wall. The numerical results are also compared with experimental measurements; they indicate similar filling processes.

Keywords: Oval disk-shaped; Inlet velocity; Wall adhesive condition; Meniscus

1. Introduction

In the last decade, microfluidic technologies have been one of the most interesting topics that span several disciplines. Some products have been mass-production using MEMS. Traditionally, both pressure and gravity are exploited to drive the flow of liquid in channels. In micro-scale systems, the flow characteristics vary among the channels because the surface-to-volume ratios exceed those in macro-systems. One of the most well-known phenomena is the surface tension effect, which is typically negligible in macro-scale systems. Microfluidic approaches that are based on surface tension have many advantages, including lower power consumption, simple machining and a lack of moving parts. Hydrophobic valves [1], micro-injection molding [2], flow switches [3], liquid metering [4] and surface tension-powered self assembly [5] have been developed. Studies of surface tension-driven flow in microchannels have been conducted. Some have dealt with the flow characteristics of liquid in channels as the cross-sections are increased. Man et al. [6] proposed several passive gating devices that exploit surface tension to stop flows in capillary tubes without the need for any moving part. They analyzed the flow characteristics of a liquid without any driving force except surface tension. The pressure barrier that arose when the channel cross-section changed sharply was determined. Kim et al. [2] studied filling with a pressure-driven flow, and the mechanism by which the flow exist from the channel. The filling flows in microchannels, driven by various forces, were studied. Some researchers [2] studied liquid filling in the cases of various pressure heads. Their results have established a linear relationship between the dimensionless pressure and the capillary number, which is the ratio of the shear force to the surface tension. Yang et al. [7] used the marching velocity or position of the meniscus front, which was driven by the capillary force and the gravitational effect, to measure the surface energy. They proposed a one-dimensional mathematical model to measure the liquid-filling behavior. Wei et al. [8] studied the process of the filling of the gap with liquid between the lens and the moving wafer, to elucidate the feasibil-

* Corresponding author. Tel.: +886 35914361; fax: +886 35910047.
E-mail address: chaucer@love.url.com.tw (J.J. Chen).

0924-4247/$ – see front matter © 2006 Elsevier B.V. All rights reserved.
doi:10.1016/j.sna.2006.03.003

ity of immersion lithography. They established that the capillary number is the key nondimensional parameter that governs passive filling. Lower contact angles tend to promote rapid filling in all cases. The filling by liquid flows of various configurations of micro-reservoirs was demonstrated and the wall surface property was emphasized. The network of microchannels and micro-wells is the main passive component of a microfluidic device. Tseng et al. [9] investigated the process by which a liquid slug was blown by an air flow that moves in and out of the micro-reservoir. The results indicate that the success of reservoir-filling depends strongly on the designs of the hydrophilic wall surface and the wall shape/size of the flow network. The implementation of immersion lithography depends on eliminating the air/lens boundaries that currently exist in the optical path. Wei et al. [10] studied the entrapment of air bubbles in the wafer as a free surface moved through the gap, during the filling process. The results show that certain flow conditions, surface properties and geometry can result in air's remaining in micro-reservoirs. However, the ranges of the parameters that cause air to be trapped have not been examined. In all of the aforementioned studies, the effects of inlet velocity on flow characteristics were not investigated. However, the flow rate was typically regarded as one of the key parameters in many microfluidic devices. These studies sought to obtain the flow characteristics of the filling liquid when the wall of the micro-reservoir was straight. The effect of the curved wall on the progress of the flow has not been studied in detail. A rotation micro-mixer has been proposed to increase the mixing efficiency; its helical shape was responsible for the rotational flow in the mixer segments [11]. The shape of the wall may affect the meniscus, so the success of the filling depends strongly on this effect. Successful filling by the liquid flows of microchannels or micro-chambers is not as easy as that of a macro-scale system because the surface effects are significant [3]. If filling is poor, then air may become entrapped in the micro-systems, degrading the functions of the systems. However, a systematic relationship among the fluid properties and operating parameters that govern the trapping of air has not been identified. Molecules in the liquid state exert strong attractive forces on each other. Surface tension, a cohesive force, arises from attractive forces among the molecules in a fluid, whereas an adhesive force to the wall acts on the fluid interface at the point of contact with the wall. Surface tension causes the surface of a liquid to act like an elastic sheath, minimizing the surface area of the liquid to minimize the energy of the fluidic system. Therefore, understanding the effects of surface tension, adhesion and inertia on fluid flows in microchannels is of marked importance in the related fields of science, medicine and engineering.

This work numerically establishes the filling processes of the liquid in an oval disk-shaped micro-chamber by considering micro-chambers with inlets and outlets of various widths, fabricated using MEMS technology. Two-dimensional time-variant fluid fields are adopted to describe the flow characteristics in micro-systems. The effects of non-dimensional parameters such as the Reynolds number and the Weber number, both related to the inlet velocity, as well as the wall adhesive conditions, on flow characteristics are studied. The fraction of the volume of each computational cell in the grid that is occupied by liquid fluid is determined to trace the gas–liquid interface during filling. The effects of the width of the microchannels in a circular disk-shaped chamber and those of the lengths of the semi-major and semi-minor axes of an oval disk-shaped chamber on the filling process are given in terms of the motion of the gas–liquid interface. Finally, flow experiments are conducted and the results compared with those of numerical simulations.

2. Mathematical model and numerical methodology

In this work, the filling processes of a liquid inside an oval or a circular disk-shaped micro-chamber, inlet pumping at a particular velocity for various values of geometrical and/or operational parameters are studied. Numerical simulations are conducted to elucidate the motion of a liquid flow inside the microchannels and the oval disk-shaped micro-chamber, as presented in Fig. 1. The channel and the chamber height are assumed to be much smaller than the chamber diameter and the chamber semi-major axis.

The governing equations comprise conservation of mass and momentum, and a scale function, F, of the liquid volume fraction inside a computational cell. The conservation equations of mass and momentum are solved to yield the motion and the shape of the gas–liquid interface. The equation of conservation of mass, also known as the continuity equation or the law of conservation of mass, states that the rate of accumulation of mass per unit volume plus the net flow rate of mass efflux per unit volume equals zero. The continuity equation can be expressed as follows:

$$\frac{\partial \rho}{\partial t} + \nabla \cdot (\rho \vec{U}) = 0 \tag{1}$$

where ρ is the fluid density, $\vec{U}$ the fluid velocity vector, and t is the time.

The momentum equation for a continuum is the analogue of Newton's second law for a point mass. The momentum principle states that the rate of change of linear momentum of material in a region equals the sum of the forces on that region. Two such forces may be included—body forces, which act on the bulk of the material in the region, and surface forces, which act on the boundary surface. The momentum equation is

$$\frac{\partial \rho \vec{U}}{\partial t} + \nabla \cdot (\rho \vec{U} \vec{U}) = -\nabla P + \nabla(\mu \nabla \vec{U}) + \vec{F}_{\mathrm{sv}} \tag{2}$$

where P is the pressure and μ is the viscosity of the fluid. The last term on the right-hand side of Eq. (2) is the volumetric surface tension which can be calculated using the continuum surface force (CSF) model. Surface tension-driven flows are source-

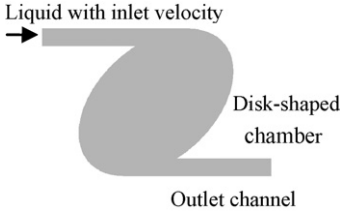

Fig. 1. Physical model.

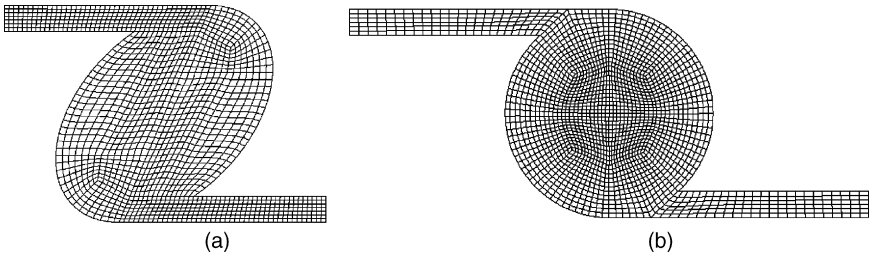

Fig. 2. The grid systems of the computation domain for (a) oval and (b) circle disk-shaped chambers.

term dominated, and convergent solutions become difficult to obtain numerically.

A finite element approach was adopted using computational fluid dynamics software (CFD-ACE(U), CFD Research Corporation, CA, USA) to model the progress of a gas–liquid free surface. The method comprises the volume-of-fluid (VOF) method, the interface tracking technique and the CSF surface tension model [12]. The characterizing feature of the VOF approach is that the distribution of the second fluid (such as water) in the computational grid is accounted for using a single scalar field variable, F. This scalar function of the liquid volume fraction is the fraction of the volume of each computational cell in the grid that is occupied by liquid fluid. Therefore, F is one in cells that contain only liquid fluid, and zero in cells that contain only gas. A cell that contains an interface would have an F of between zero and unity. Given a flow field and an initial distribution of F over the grid, the evolution of the volume fraction distribution is determined by solving the passive transport equation:

$$\frac{\partial F}{\partial t} + \vec{U} \cdot \nabla F = 0 \tag{3}$$

This equation must be solved together with Eqs. (1) and (2) to achieve computational coupling between the velocity field solution and the liquid distribution.

The height of the system is assumed to be much smaller than the diameter and the semi-major axis of the chamber. A two-dimensional time-variant fluid field is adopted to specify the flow characteristics of micro-systems. The classification of the VOF method as a volume tracking method follows directly from the use of F to describe the distribution of liquid and to yield the liquid volume evolution. One consequence of the purely volumetric representation of the phase distributions is that the interface between gas and liquid is not uniquely defined. Therefore, it must be dynamically reconstructed from the distribution of F. In this work, an upwind scheme with piecewise linear interface construction (PLIC) is adopted to determine the flux of fluid from one cell to the next and the curvatures of the surface. In the PLIC scheme, each cell has a unique surface normal that can be adopted to determine the surface curvature from cell to cell, enabling the surface tension forces of the free surfaces to be calculated and added. This work considers two configurations of the flow systems. The first comprises inlet/outlet microchannels and a circular disk-shaped micro-chamber with an adhesive wall surface. In the second of the micro-chamber is an oval disk-shaped chamber (cf. Fig. 2). The grid systems in the computational domain are selected to ensure the orthogonality, the smoothness and the low aspect ratios that prevent numerical divergence. Poor orthogonality most directly influences the accuracy of the flux calculations, whereas poor smoothness and high aspect ratios most directly affect the accuracy of the surface reconstruction.

3. Fabrication process and flow visualization

Fig. 3 presents the flow device fabricated by MEMS technology. The microchannels and micro-chamber are fabricated in silicon wafer by standard photolithography and dry etching technology, and are covered with a Pyrex glass chip using anode bonding technology. The initial silicon wafer is a silicon substrate polished on both sides with a diameter of four inches. A thin film (500 nm) of aluminum is deposited on the silicon wafer by thermal evaporation. Photoresist is applied to the surface and spun, yielding a resist film. Each wafer is then soft baked, exposed to light through a mask, and developed in a standard developer solution. Next, the wafer is baked in an oven and the exposed aluminum is removed by immersion in an

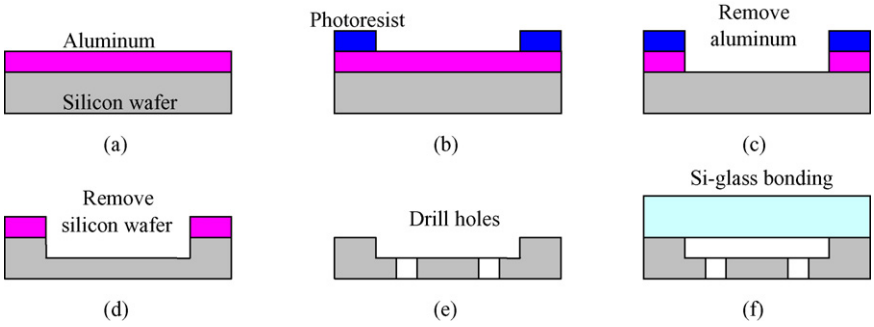

Fig. 3. Fabrication process of microchannels and micro-chamber.

aluminum etching solution until all of the exposed aluminum has been removed. The accessible silicon wafer is then etched by HDP-RIE. The aluminum layer is again removed by etching solution. The inlet/outlet holes are drilled using a supersonic vibrating driller on opposite sides of a single silicon wafer. The wafer is rinsed in deionized water, air dried and oven-dried. Finally, a Pyrex glass, with a diameter of four inches, is cleaned and anodically bonded to the silicon wafer. Then, the wafer is diced into individual samples and the process is complete.

The micro-chamber is designed to study the effects of various forces such as inertia force, adhesion force and surface tension on the filling characteristics in a chamber, with reference to geometric effects. The working fluid enters an inlet channel; flows through the oval chamber; finally exists through an outlet channel. The filling patterns are dynamically recorded using a computer system using a high speed camera and a graphic grabber card (VCD-Gear TV Plus) at rates of 125, 250, 500 and 1000 fps. The rate depends on the flow inlet velocity.

4. Results and discussion

Two configurations of the flow network system are considered. The microchannels are either 100 or 50 μm wide and the circular disk-shaped micro-chamber has a diameter 800 μm. These dimensions correspond to angles between the microchannel and the micro-chamber at the intersection of 138.6° and 151°, respectively. The microchannels are 100 μm wide in the oval disk-shaped micro-chamber for various lengths of the semi-major and semi-minor axes. The microchannel is 80 μm deep. The chambers may have hydrophilic or hydrophobic surfaces. The contact angles of the air–water interface on the solid surface are 30°, 90° and 150° to simulate filling under various surface conditions and to elucidate the mechanism by which the front changes and the air is trapped in the chamber. In the following, the effects of the various parameters on the motion and the shape of the air–water interface in a circular disk-shaped chamber are studied first. Then, the effects of changes in the length(s) of the semi-major axis and/or the semi-minor axis of an oval disk-shaped chamber on the flow characteristics are studied. The above values of the parameters are used unless otherwise stated.

Figs. 4–8 plot the effects of various inlet velocities on the filling process for a microchannel width of 100 μm. They show not only the process of filling through the micro-chamber, but also the change in the shape of the liquid front. In this work, regions of liquid occupancy and gas have different colors. Weber numbers of 1.38, 0.345 and 0.0138, and Reynolds numbers of 100, 50 and 10, are considered, corresponding to inlet flow velocities of 1, 0.5 and 0.1 m/s, respectively. The Weber number is the ratio of the inertia to the surface tension, and is given by $We = \rho U_{\text{inlet}}^2/\sigma$. The Reynolds number is the ratio of the inertia to the viscosity and is given by $Re = U_{\text{inlet}} W/\nu$ where U_{inlet} is the inlet flow velocity and W is the width of the microchannel. ν and σ are the kinematic viscosity and the surface tension of the liquid, respectively. The contact angle of the gas–liquid interface on a solid surface is taken to be 90°. In Fig. 4, the fluid enters an inlet channel at a pumping velocity of 0.1 m/s. Fig. 4(a)–(f) presents results for $t = 1.02 \times 10^{-2}$, 1.75×10^{-2}, 2.47×10^{-2}, 4.37×10^{-2}, 5.25×10^{-2} and 6.25×10^{-2} s, respectively. The liquid flows forward and approaches the entrance of the chamber. When the gas–liquid interface reaches the sharp corner, the meniscus near this corner stops moving forward and remains at this point until the bulk of the flow has advanced sufficiently, allowing the meniscus to bulge sufficiently over the corner so that the contact angle at the edge reaches 90°. The adhesive force between the liquid and the solid wall is established to establish a capillary pressure barrier that stops the flow. At this

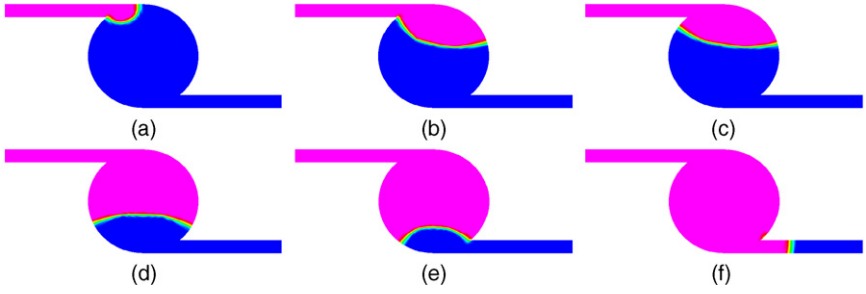

Fig. 4. Filling process for inlet velocity of 0.1 m/s.

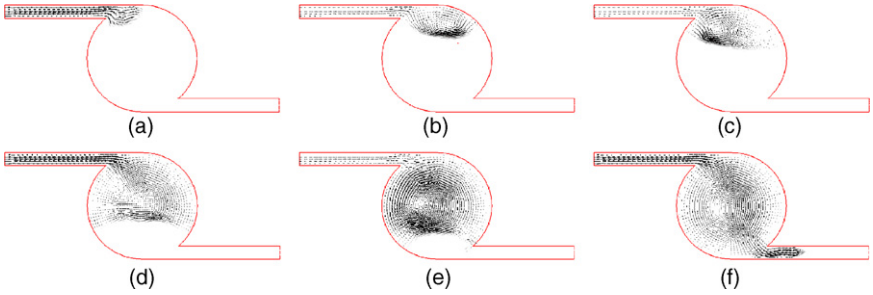

Fig. 5. Velocity vector plot of filling process for inlet velocity of 0.1 m/s.

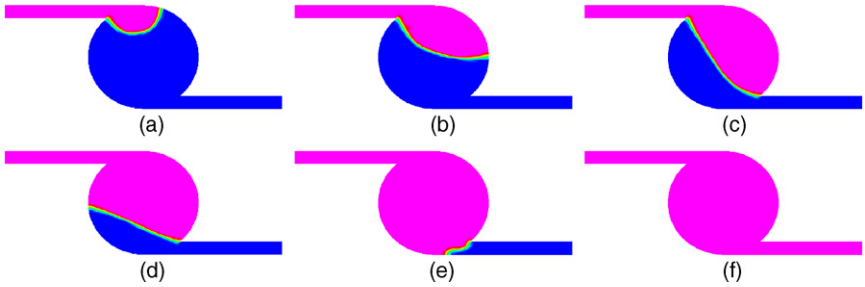

Fig. 6. Filling process for inlet velocity of 0.5 m/s.

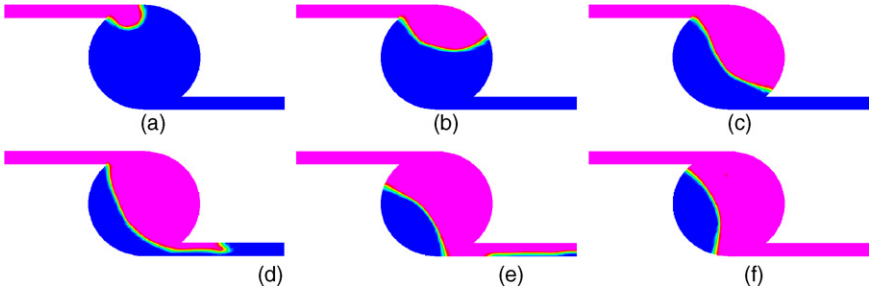

Fig. 7. Filling process for inlet velocity of 1 m/s.

point, the liquid meniscus must change angle to adopt the equilibrium contact angle at the slanted walls, and then this side of the meniscus descends down the side of the chamber and along the surface. The other side of the meniscus keeps moving forward until it reaches the entrance of the chamber, because the wall of the inlet channel is tangential to the wall of the chamber and the inertia force continues to drive the liquid flow forward. Then, the flow leaves the inlet channel, wetting the side surface. This change in the angle between the microchannels and the micro-chamber at the intersection increases the gas–liquid area to more than the solid–liquid area for a given volume change, resulting in a negative opposing pressure. The surface tension of the meniscus and the liquid pumping force overcome this capillary pressure barrier that develops when the cross-section of the channel changes abruptly, establishing a positive pressure that pulls the liquid into the micro-chamber. *We* is small, so the surface tension dominates the flow mechanism. As the liquid flows into the chamber, the flow front becomes convex because of the adhesive condition of the wall. The curvature of the wall of the chamber changes the shape of the front such that it becomes flat when the liquid occupies almost half of the area of the chamber. Then, the shape becomes concave. The variations in the shape of the front are related directly to the properties of the wall. The convex shape is maintained for longer if a hydrophobic wall property is applied. When the liquid meniscus reaches the outlet channel, one side of the liquid meniscus reaches the sharp corner, and it stops moving forward. The other side of the meniscus continues to flow through the chamber. When the angle of the liquid meniscus changes to the equilibrium contact angle at the sharp corner, the gas–liquid interface exits through the outlet channel. The results indicate that the changed angles at the entrance and the exit of the chamber are closely related to the flow progression when geometric changes occur at the connections between the chamber and the channels. Finally, the liquid completes the filling process. Fig. 5 presents the simulated velocity vector as the liquid enters the micro-chamber presented in Fig. 4. When the gas–liquid interface reaches the sharp corner, a negative opposing pressure develops and a small clockwise vortex is formed around this sharp corner. At the other side of the meniscus, the liquid keeps moving forward after it has reached the entrance of the chamber because of inertia. The inertial effect is not obvious, so a large counterclockwise vortex

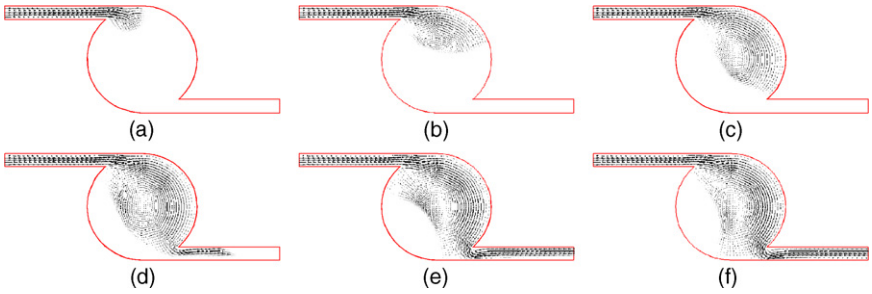

Fig. 8. Velocity vector plot of filling process for inlet velocity of 1 m/s.

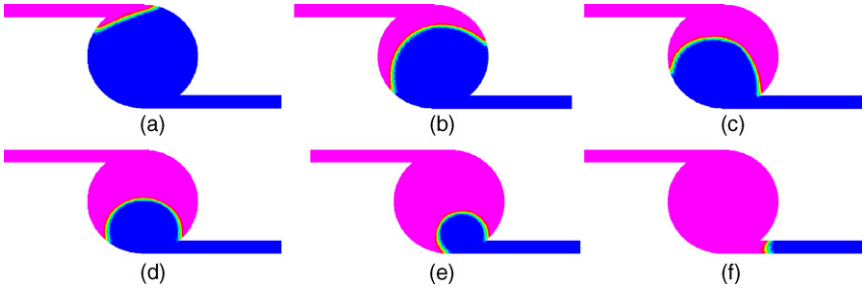

Fig. 9. Filling process for contact angle of 30°.

is formed and is presented in Fig. 5(b). When the liquid flows into the chamber, the counterclockwise vortex disappears and another clockwise vortex is formed by the circular structure of the micro-chamber. During the remainder of the filling process, the clockwise vortex shifts toward the central part of the micro-chamber. When the filling process is complete, the vortex shifts to the left part of the micro-chamber.

Re increases with the inlet velocity and the inertia force becomes dominant, as presented in Fig. 6. Fig. 6(a)–(f) presents results for $t = 2.85 \times 10^{-3}$, 5.37×10^{-3}, 7.54×10^{-3}, 9.45×10^{-3}, 11.76×10^{-3} and 13.49×10^{-3} s, respectively, at an inlet velocity of 0.5 m/s. As the free surface reaches the sharp corner at the entrance of the chamber, the gas–liquid interface near this corner stops moving. The other side of the free surface moves until it reaches the other sharp corner at the exit of the chamber. The strong inertial force causes the interface to remain convex. Then, the side of the interface that stopped at the corner before it begins to move again. Finally, the filling process is finished without the entrapment of air bubbles. In Fig. 6, the wave front shape is changed from convex to flat and then to concave. The competition between inertia and adhesion causes the shape to be linear for a long time. However, significantly increasing the inlet velocity may result in the entrapment of air. Fig. 7 presents the results for an even higher inlet velocity of 1 m/s. Fig. 7(a)–(f) plots results for $t = 1.13 \times 10^{-3}$, 2.32×10^{-3}, 3.54×10^{-3}, 4.63×10^{-3}, 5.80×10^{-3} and 7.50×10^{-3} s, respectively. The inertial force is much important when the Reynolds number is 100. When the meniscus is attached to the sharp corner of the feature, it cannot achieve the required contact angle with the wall and so does not flow into the chamber before the meniscus enters the outlet channel. When *Re* is increased to a much higher value, the inertial force causes the meniscus to move faster; overcomes the flow resistance at the corner easily, and drives the fluid flowing into the outlet. Therefore, air is trapped in the feature and remains after the flow has passed over the area of interest. When the liquid meniscus reaches the outlet channel, the entrapment of air is strongly related to the gas–liquid interface and the flow characteristics. Fig. 8 plots in detail the simulated velocity vector as the liquid passes the micro-chamber presented in Fig. 7. When the free surface reaches the sharp corner at the entrance of the chamber, a small clockwise vortex is formed around this sharp corner. The larger inertia force causes the interface to proceed and another large clockwise vortex to form, as presented in Fig. 7(b). When the interface flows into the outlet channel, this vortex shifts around the central portion of the micro-chamber. The large empty region formed near the left part of the micro-chamber is such that no liquid is in this region, indicating that the filling of the system is incomplete.

Figs. 9 and 10 plot the results concerning the motion of the gas–liquid interface at various liquid/substrate contact angles. The diameter of the circle chamber is taken to be 800 μm, and the width of the channels is 100 μm. A Weber number of 0.0138 and a Reynolds number of 10 are used, corresponding to an inlet flow velocity of 0.1 m/s. The surface tension force dominates these two cases. Fig. 9 presents the progress of the flow in a circular chamber with a liquid/substrate contact angle of 30°. Fig. 9(a)–(f) present results for $t = 1.10 \times 10^{-2}$, 2.35×10^{-2}, 3.03×10^{-2}, 4.09×10^{-2}, 5.00×10^{-2} and 6.03×10^{-2} s, respectively (for a hydrophilic wall OR under a hydrophilic wall condition), the flow front keeps moving into the chamber without stopping, because of surface tension and inertia. When the surface tension dominates, the fluid flows into the chamber, wetting the side surface, and the effect of a capillary pressure barrier does not remain obvious. When the liquid moves into the chamber, the increase in the cross-sectional area of the chamber reduces the inertia. The

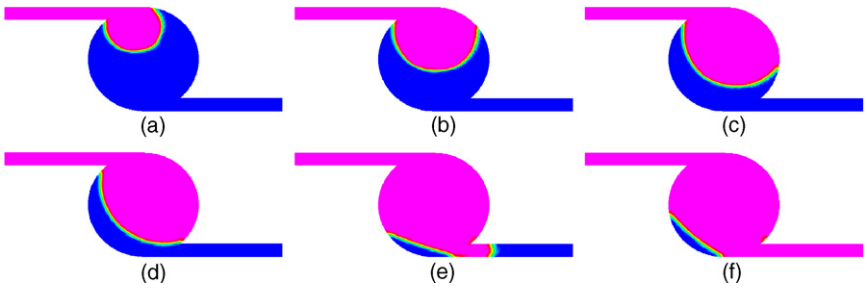

Fig. 10. Filling process for contact angle of 150°.

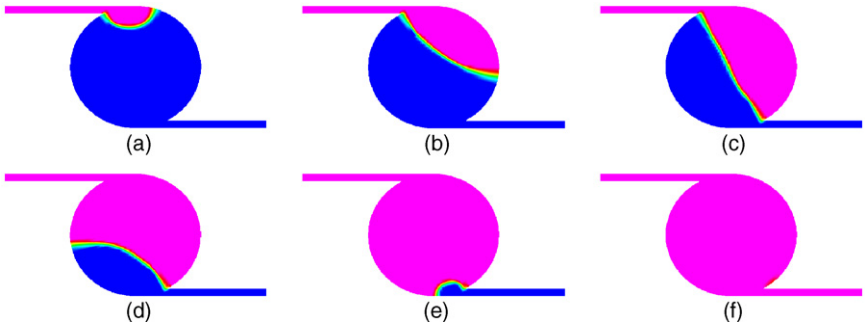

Fig. 11. Filling process for the width of the channels of 50 μm.

interface stops moving at the sharp corner near the exit of the chamber and its angle changes to the contact angle. The interface retains its concave shape throughout the filling process. The same feature profile is used in Fig. 10, but the liquid/substrate contact angle is increased to 150°. Fig. 10(a)–(f) plots results for $t = 1.95 \times 10^{-2}$, 3.16×10^{-2}, 4.15×10^{-2}, 4.74×10^{-2}, 5.88×10^{-2} and 6.11×10^{-2} s, respectively. Given a hydrophobic wall, the front is convex as the liquid flows through the chamber without wetting the side surface. After the meniscus reaches the sharp corner near the inlet or the outlet channel, it remains at the corners until the bulk of the flow has sufficiently advanced. The liquid flow is still driven by the inertia, so the meniscus bulges over the whole chamber. Given a hydrophobic wall with a contact angle of 150°, the wave front becomes attached to the wall before the meniscus stretches across the whole chamber. The meniscus bulges sufficiently over the sharp corner near the outlet channel so the contact angle at the edge reaches 150°. The interface descends along the outlet channel so air is entrapped.

The effect of the width of the channels at an inlet flow velocity of 0.1 m/s is parametrically studied. Fig. 11 presents the results when the width of the channels is reduced to 50 μm. Fig. 11(a)–(f) plots results for $t = 2.63 \times 10^{-3}$, 5.17×10^{-3}, 6.94×10^{-3}, 8.15×10^{-3}, 10.21×10^{-3} and 11.26×10^{-3} s, respectively. *We* equals 0.0069. *Re* equals 5. The change in the angle between the microchannels and the micro-chamber at the intersection is 151°, which angle is larger at this width than for an inlet width of 100 μm. The liquid/surface contact angle is maintained at 90°. After the gas–liquid interface enters the chamber, one end of the meniscus stops at the sharp corner and the other end of the meniscus keeps moving. The change in the angle between the microchannels and the micro-chamber is large so the meniscus stays at this point for a longer time with a larger pressure barrier. When the interface reaches the other corner, the meniscus stops and the other end of the meniscus begins to move again. The flow fills the chamber without the entrapment of any air because the inertia force is low, because the *Re* number is small.

The effects of the semi-major axis and the semi-minor axis of an oval disk-shaped chamber on the flow characteristics are studied with an inlet velocity of 0.1 m/s and are plotted in Figs. 12 and 13. The flow system of interest comprises microchannels with a width of 100 μm and an oval disk-shaped chamber with a hydrophilic surface. The contact angle of the gas–liquid interface on the solid surface is taken to be 30°. Two sets of lengths of the semi-major and semi-minor axes of the oval disk-shaped chamber are 500 μm/320 μm and 640 μm/250 μm, so the cross-sectional area of the disks equals that of the circular chamber with a diameter of 800 μm. The angle between the semi-major axis and the horizontal line is 45°, whereas those between the microchannels and the micro-chamber at the intersection are 146.1° and 148.3°. Fig. 12(a)–(f) plots the results for $t = 0.67 \times 10^{-2}$, 1.62×10^{-2}, 2.79×10^{-2}, 3.61×10^{-2}, 4.35×10^{-2} and 5.07×10^{-2} s, respectively. Fig. 13(a)–(f) plots results for $t = 0.67 \times 10^{-2}$, 1.09×10^{-2}, 2.39×10^{-2}, 3.41×10^{-2}, 4.53×10^{-2}, and 4.76×10^{-2} s, respectively. The circular disk-shaped chamber is regarded as a special case of an oval disk-shaped chamber with equally long semi-major and

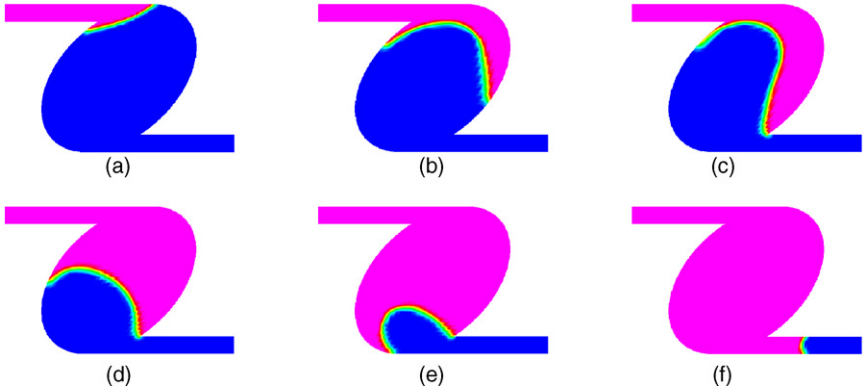

Fig. 12. Filling process for the oval disk-shaped chamber with the semimajor and semiminor axes being 500 and 320 μm.

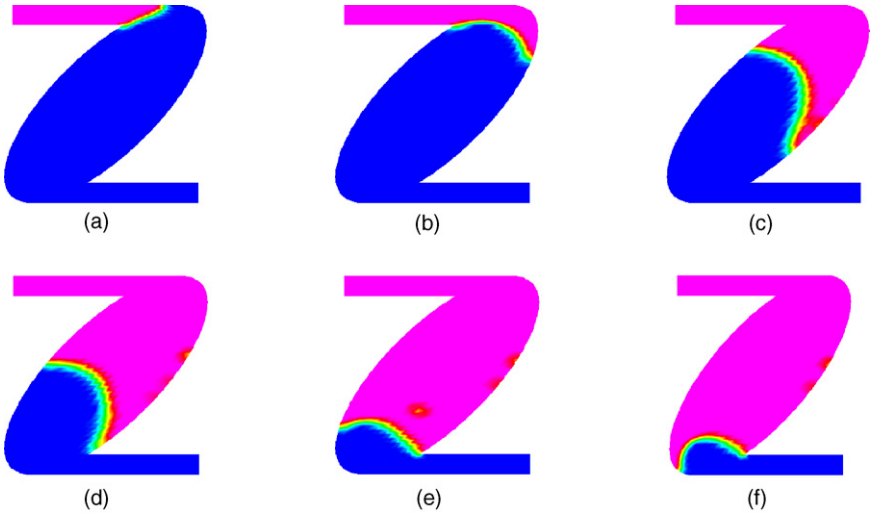

Fig. 13. Filling process for the oval disk-shaped chamber with the semimajor and semiminor axes being 640 and 250 μm.

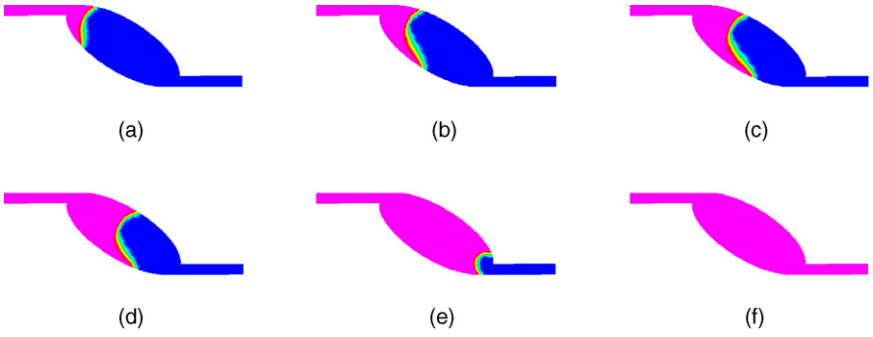

Fig. 14. Filling process for the oval disk-shaped chamber with the semimajor and semiminor axes being 640 and 250 μm.

semi-minor axes. A longer semi-major axis corresponds to a greater change in the angle between the microchannels and the micro-chamber. The capillary pressure barrier becomes more difficult to overcome; the interface must change and the angles reach the equilibrium contact angle at the slanted walls. The flow patterns in Figs. 12 and 13 resemble that in Fig. 9. The figures indicate that no difference between the variations of the flow front in these cases is evident. Fig. 14 plots the various angles between the semi-major axis and the horizontal line at an inlet velocity of 0.1 m/s, a contact angle of the gas–liquid interface on the solid surface of 30° and a channel width of 100 μm to study the effects of a change in the angle between the microchannels and the micro-chamber at the intersection. The lengths of the semi-major and semi-minor axes of the oval disk-shaped chamber are chosen to be 640 and 250 μm, and the angle between the semi-major axis and the horizontal line is set to 150°. The angle between the microchannels and the micro-chamber at the intersection in this case is 110.4°. Fig. 14(a)–(f) plots results for $t = 0.53 \times 10^{-2}$, 1.32×10^{-2}, 2.41×10^{-2}, 3.25×10^{-2}, 4.11×10^{-2} and 5.01×10^{-2} s, respectively. A larger angle between the semi-major axis and the horizontal line corresponds to a smaller change in the angle between the microchannels and the micro-chamber. The interface reaches the sharp corner and advances sufficiently over the corner without any difficulty, because the capillary pressure barrier is small, as revealed by a comparison with Fig. 13. Therefore, the formation of air bubbles can be avoided. In cases with a liquid/substrate contact angle of 150° and geometric profiles similar to those in Fig. 14, even for a hydrophobic wall, the filling process can still be completed successfully.

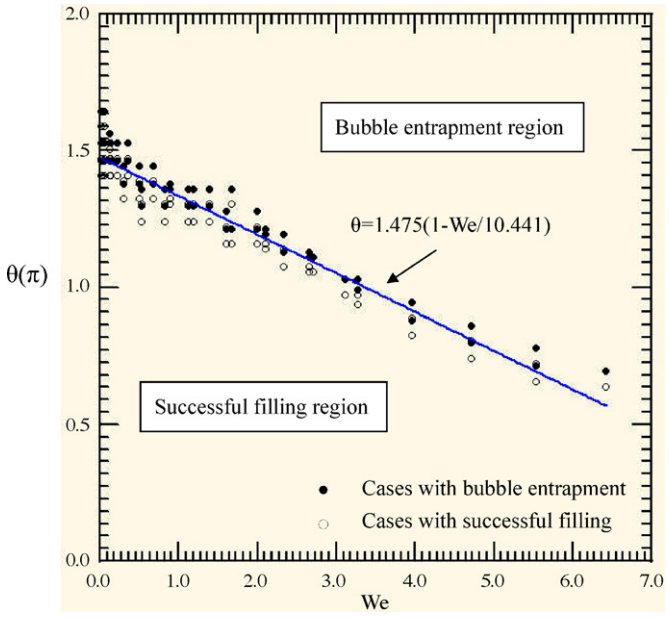

Fig. 15. A systematic relationship with the onset of bubble creation.

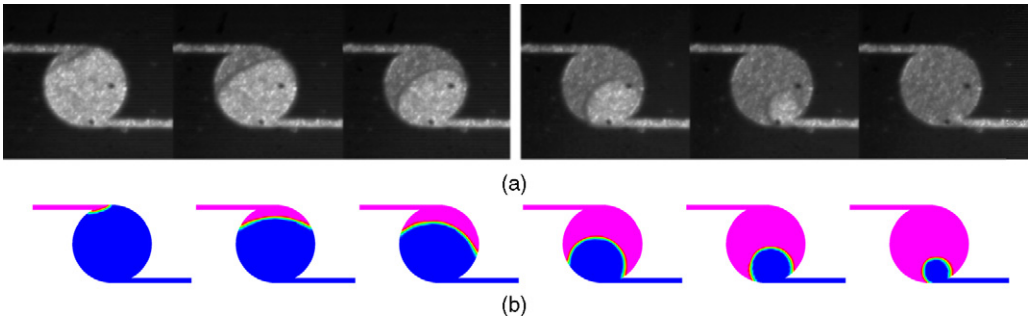

Fig. 16. (a) Photographs of a microchannel device showing liquid filling process. (b) Computational results corresponding to (a).

In the transient microfluidic filling processes, many forces – inertia, adhesion and surface tension – affect the flow characteristics. The simulated results indicate that the motion of the gas–liquid interface significantly affects the formation of the air bubble. The entrapment of air could in the chamber under strong inertial force could not be prevented; the angle between the channels and the chamber at the intersection changes significantly and/or the chamber wall exhibits hydrophobicity. Extensive numerical simulations were conducted by changing the physical characteristics of the fluids, the geometry of the micro-chamber, the inlet velocities and other factors. The numerical analysis establishes a systematic relationship between the bubble creation and the Weber number, the liquid/substrate contact angle and the change in the angle between the microchannels and the micro-chamber at the intersection. Fig. 15 shows a linear relationship between the bubble creation and *We*, the sum of the liquid/substrate contact angle and the change in the angle between the microchannels and micro-chamber at intersection. The linear relationship is given by

$$\theta = a\left(1 - \frac{We}{b}\right)$$

where θ is the sum of the liquid/substrate contact angle and the angle between the microchannels and micro-chamber at intersection, divided by π. a is around 1.475, and b is around 10.441. On the top right-hand part of this parametrical map is a bubble entrapment region where air is entrapped during filling when the physical properties of the fluids and the operating parameters inside the region are determined. The bottom-left of this figure presents a successful filling region, in which the liquid filling process is completed when the physical properties of the fluids and the operating parameters are located inside the region. For a constant Weber number, the air entrapment depends on the adhesive properties of the wall and geometric changes in the micro-chamber. The inertial effects drop the Weber number. The surface tension of the meniscus and the liquid pumping force overcomes the large capillary pressure barrier. Then, the liquid/gas interface moves and bulges sufficiently over the sharp corner at the larger θ without the entrapment of any air bubbles. When the Weber number is larger, the inertial force becomes is more important. When the meniscus is attached to the sharp corner of the feature, achieving the required contact angle relative to the wall becomes more difficult as the contact angle increases. Overcoming a large capillary pressure barrier becomes more difficult as the change in the angle between the microchannels and micro-chamber at the intersection increases. Therefore, air is not trapped in the feature only at small θ. This relationship can help researchers who are interested in designing microfluidic devices by indicating how effectively to fill the micro-chamber.

In Fig. 16, Pyrex glass is used as a cover under which the micro-system is fabricated on a silicon wafer using MEMS technology. This glass is almost completely transparent in the visible spectrum. Flow experiments are conducted at least four times, under the same condition, to confirm repeatability. In each experiment, the total filling time is measured with a deviation of the order of 0.001 s. The experimental observations described below were repeatable. Fig. 16 presents many experimental results obtained in a micro-chamber with a diameter of 800 μm and the microchannels are 50 μm wide and 80 μm deep with an inlet velocity of 0.1 m/s. The results are confirmed by numerical simulation and flow visualization. The numerical results are also compared with experimental measurements and reveal similar filling processes. Numerical results are listed from left to right for $t = 2.13 \times 10^{-3}$, 5.21×10^{-3}, 6.45×10^{-3}, 7.83×10^{-3}, 10.02×10^{-3} and 12.11×10^{-3} s, respectively, at a liquid/surface contact angle of 30°. The flow front shapes differ between numerical simulations and flow visualizations, especially in regions in which the flow front enters the chamber after it passed around the sharp corner, perhaps because a reduced simulation model (a three-dimensional model reduced to a two-dimensional model) was used; because of non-smoothness of the chamber and the channel surface, or because of the non-uniformity of the flow rate during the experiments.

5. Conclusions

In this work, the filling processes of the liquid in an oval disk-shaped micro-chamber were numerically studied using micro-chambers with inlets and outlets of various widths, fabricated on a silicon wafer by standard MEMS technology and covered with a Pyrex glass chip using anode bonding technology. A two-dimensional computational model is proposed to trace the gas–liquid interface, because the height of the channels and the chamber is much smaller than the chamber diameter and the chamber semi-major axis. The results specify the motion of the gas–liquid interface. Fluid flow simulations are conducted to

study the progress of the liquid meniscus and/or the entrapment of air bubbles in the micro-chamber. During filling, competition among the inertia, adhesion and surface tension determined the front shape. Clearly, the wall adhesive conditions and the curve walls of the chamber significantly affect the shape of the gas–liquid interface during filling, and the variations of the shape also depend on the Reynolds number and the Weber number. The effects of the change in the channel widths of a circular chamber and of changes in the lengths of the semi-major and semi-minor axes of an oval chamber on the filling process are also studied. The aforementioned geometric changes change the angle between the microchannels and the micro-chamber at the intersection and significantly influence the filling of the micro-chamber with liquid. Evidently, the progress of the gas–liquid interface significantly affects the formation of air bubbles; the entrapment of air cannot be prevented in the chamber when a strong inertia force is applied, large angular changes between the channels and the chamber at the intersection are adopted, and/or the inside of the chamber wall exhibits hydrophobicity. The numerical results indicate linear relationships between the formation of bubble and both the Weber number and the sum of the liquid/substrate contact angle and the change in the angle between the microchannels and the micro-chamber at the intersection. Finally, the numerical results are compared with experimental measurements and exhibit similar filling processes.

References

[1] Y. Feng, Z. Zhou, X. Ye, J. Xiong, Passive valves based on hydrophobic microfluidics, Sens. Actuators A 108 (2003) 138–142.
[2] D.S. Kim, K. Lee, T.H. Kwon, S.S. Lee, Microchannel filling flow considering surface tension effect, J. Micromech. Microeng. 12 (2002) 236–246.
[3] B. Zhao, J.S. Moore, D.J. Beebe, Surface-directed liquid flow inside microchannels, Science 291 (2001) 1023–1026.
[4] K. Handique, D.T. Burke, C.H. Mastrangelo, M.A. Burns, Nanoliter liquid metering in microchannels using hydrophobic patterns, Anal. Chem. 72 (2000) 4100–4109.
[5] R.R.A. Syms, E.M. Yeatman, V.M. Bright, G.M. Whitesides, Surface tension-powered self-assembly of microstructures—the state-of-the-art, J. Microelectr. Syst. 12 (2003) 387–417.
[6] P.F. Man, C.H. Mastrangelo, M.A. Burns, D.T. Burke, Microfabricated capillarity-driven stop valve and sample injector, in: Proceedings of the 11th Annual International Workshop on Micro-Electro Mechanical Systems, MEMS '98, Heidelberg, Germany, January 25, 1998, pp. 45–50.
[7] L.J. Yang, T.J. Yao, Y.C. Tai, The marching velocity of the capillary meniscus in a microchannel, J. Micromech. Microeng. 14 (2004) 220–225.
[8] A.C. Wei, G.F. Nellis, A.Y. Abdo, R.L. Engelstad, C.F. Chen, M. Switkes, M. Rothschild, Microfluidic simulations for immersion lithography, J. Microlith. Microfab. Microsyst. 3 (2004) 28–34.
[9] F.G. Tseng, I.D. Yang, K.H. Lin, K.T. Ma, M.C. Lu, Y.T. Tseng, C.C. Chieng, Fluid filling into micro-fabricated reservoirs, Sens. Actuators A 97/98 (2002) 131–138.
[10] A.C. Wei, G. Dicks, A.Y. Abdo, G.F. Nellis, R.L. Engelstad, J. Chang, E. Lovell, W. Beckman, Predicting microfluidic response during immersion lithography scanning, in: Proceedings of the 20th European Conference on Mask Technology for Integrated Circuits and Microcomponents, Proc. SPIE 5504 (2004) 155–163.
[11] S.J. Park, J.K. Kim, J. Park, S. Chung, C. Chung, J.K. Chang, Rapid three-dimensional passive rotation micromixer using the breakup process, J. Micromech. Microeng. 14 (2004) 6–14.
[12] CFDRC Module Manual, CFD Research Corporation, 2002.

Biographies

Jyh-Jian Chen received the BS degree, the MS degree and the PhD degree in mechanical engineering from National Chiao Tung University, Taiwan, ROC, in 1991, 1992 and 1999, respectively. In 1999–2004, he worked as an associate researcher at Precision Instrument Development Center, Taiwan, ROC, where he focuses on the development of optomechanical systems for remote sensing applications. Since spring 2004, he has been Industrial Technology Research Institute, Taiwan, ROC, as an engineer in the Bio Microfluidic Technology Department. His research interests are microfluidics, and BioMEMS as well as computational simulation.

Wen-Zhong Liu received the MS degree in mechanical engineering from National Chiao Tung University, Taiwan, ROC, in 2002. Since spring 2004, he has been Inventec Corporation, Taiwan, ROC, as an engineer in the Safety Department. His research interests are microfabrication technologies, microfluidics, and BioMEMS as well as signal processing.

Jenn-Der Lin received the BS degree in mechanical engineering from Tamkang University, Taiwan in 1975, MS and PhD degrees in mechanical engineering from the University of Oklahoma, USA, in 1980 and 1985, respectively. After then, he has been associated with the Department of Mechanical Engineering at National Chiao Tung University (NCTU), Hsinchu, Taiwan. He is currently a professor in the Department of Mechanical Engineering at NCTU and also jointly employed as the president of National Formosa University, Huwei, Taiwan. He currently oversees graduate students in the Thermal Science Research Laboratory at NCTU, whose research activities cover a variety of areas such as the micro-scale heat transfer for ultra-fast laser heating or annealing, biothermodynamics and microfluidics in delivery system of bio-chips, as well as the impact dynamics of liquid micro-droplets on a solid surface.

Jyh-Wen Wu received the BS degree in mechanical engineering from Tatung University, Taiwan, ROC, in 1990, the MS degree and the PhD degree in mechanical engineering from National Chiao Tung University, Taiwan, ROC, in 1992 and 1999, respectively. Since winter 1999, he has been Industrial Technology Research Institute, Taiwan, ROC, as an engineer in the Bio Microfluidic Technology Department. His research interests are microfabrication technologies, microfluidics, and BioMEMS.